Nanoscale

PAPER

View Article Online
View Journal | View Issue

Cite this: *Nanoscale*, 2019, **11**, 4925

Gold nanoparticle densely packed micro/nanowire-based pressure sensors for human motion monitoring and physiological signal detection†

Shun-Xin Li,[a] Hong Xia,*[a] Yi-Shi Xu,[a] Chao Lv,[a] Gong Wang,[a] Yun-Zhi Dai[a] and Hong-Bo Sun *[a,b]

Received 20th January 2019,
Accepted 16th February 2019

DOI: 10.1039/c9nr00595a

rsc.li/nanoscale

Flexible pressure sensors have gained ever-increasing attention because of their widespread applications in wearable devices. The sensor fabrication technologies reported so far are generally complicated, limiting their industrial applications. It is therefore of great importance to develop a simple method to fabricate high-performance flexible pressure sensors. Herein, we report an approach of assembling gold nanoparticles into strictly aligned and densely stacked micro/nanowires by imprinting for flexible pressure sensors with high performance. By our method, the whole assembly process takes only 1 min. The pressure sensor exhibits a best detection limit as low as 25 Pa. The sensors could be attached to any part of the human body and are so sensitive that even pulses in different regions of the body and the differences between a pregnant woman and a nonpregnant woman could be distinguished.

Introduction

Recent years have witnessed a rapid development of soft robots, artificial intelligence and wearable health care devices.[1–3] As one of the most fundamental component parts, flexible electronic devices which exhibit sensing performance have aroused great attention and research interest.[4–7] Of all the sensing devices, pressure sensors, which can convert people's daily activities, physiological activities and other pressure stimulation information into readable signals, are of greatest importance.[5] In order to expand their application range in artificial intelligence, wearable health care devices and other industrial applications, great efforts are now being made to find a simple, low-cost and efficient fabrication strategy for high-sensitivity, high-flexibility and low-power-consumption pressure sensing devices.[8–10]

Because of their simple device structure and ease of fabrication, piezoresistivity-based pressure sensors have been studied extensively.[11,12] Functional conductive materials are generally filled into a flexible matrix to achieve flexible pressure sensors with high performance.[12] For example, by filling the conductive graphene into a 3D hollow matrix, the Zhao group had achieved a flexible pressure sensor with a high sensitivity up to 15.9 kPa^{-1}.[13] However, the preparations of the porous matrix are cumbersome and time-consuming. Moreover, the filling process of active materials into the porous matrix is rather complicated and often takes much time, leading to a long preparation cycle.[13]

From the aspect of materials, as one of the most popular multiple functional materials,[14–17] metal nanoparticles have been widely used in several fields, such as chemistry (catalyzer),[18] biomedical science (drug delivery),[19] and optics (optical switch, optical communication).[20] Owing to their great electrical conductivity, metal nanoparticles are often used as conductive paste. Despite all of these outstanding properties, metal nanoparticles have rarely been applied in flexible pressure sensors.

In order to simplify the preparation of the flexible pressure sensor, here we propose an imprinting strategy to effectively assemble gold nanoparticles into densely stacked micro/nanowires. The whole assembly process takes only 1 min. By this method, we have achieved a pressure sensor with a low limit of detection (25 Pa), low operating voltage (<0.1 V) and low power consumption (<0.8 mW). Because of its two-dimensional structure and small size, it has advantages of better robustness and easier integration than previously reported three-dimensional structure-based pressure sensors. It has excellent stability in

[a]*State Key Laboratory of Integrated Optoelectronics, College of Electronic Science and Engineering, Jilin University, 2699 Qianjin Street, Changchun 130012, China. E-mail: hxia@jlu.edu.cn*
[b]*State Key Lab of Precision Measurement Technology and Instruments, Department of Precision Instrument, Tsinghua University, Haidian, Beijing 100084, China. E-mail: hbsun@tsinghua.edu.cn*

†Electronic supplementary information (ESI) available. See DOI: 10.1039/c9nr00595a

the atmospheric environment and under humidity and can work under various conditions. In addition, because of the many contact points provided by the nanoparticle densely packed micro/nanowires, the gold nanoparticle-stacked micro/nanowire-based pressure sensors are capable of working in a low pressure regime, which is very important for their application in ultra-sensitive e-skin. Furthermore, the simple and low-cost fabrication process makes it possible for mass production for industrial applications. This kind of pressure sensor can be attached to the human body to monitor biological signals such as artery waveforms and body movements such as the bending of fingers or wrists and voice vibration, and can also be applied to a robotic hand for detecting signals of grabbing objects and other motions. Our work therefore provides a new path to the fabrication of flexible pressure sensors.

Results and discussion

The imprinting method is an effective way to control the patterns and orientation of functional materials by template restriction.[21] It has been successfully applied to achieving patterning of various materials during their self-assembly process.[22] Here we exploit this traditional imprinting method to assemble gold nanoparticles into densely packed micro/nanowires. We chose (11-mercaptoundecyl)tetra(ethylene glycol) functionalized gold nanoparticle water dispersion to prepare these densely packed micro/nanowires. The schematic diagram of the preparation process is presented in Fig. 1a–d. Firstly, a PDMS template with microchannel structures is placed to come into close contact with the substrate (Fig. 1a). In order to make sure that the PDMS template is in tight contact with the substrate, a slight pressure is applied to the PDMS template. Therefore, several separate microchannels were formed between the PDMS template and the substrate. A small amount of gold nanoparticle colloid is then dropped onto one end of the PDMS template (Fig. 1b). Owing to the capillary force, the colloid liquid is guided into the separated microchannels and gradually fills them up to form several separate liquid strips (Fig. 1c). Then, at an appropriate heating temperature, the nanoparticle dispersion liquid begins to evaporate. Because of the adsorption of the microchannel side walls, two liquid tails formed on both sides of each microchannel. During the evaporation process, the side walls of the microchannels provide deposition sites for gold nanoparticles (Fig. 1d). Thus, after a short period of time, the water molecules in the gold nanoparticle dispersion evaporate completely, leaving micro/nanowires stacked by gold nanoparticles on both sides of the microchannel walls (Fig. 1e). After the PDMS template is removed, many gold nanoparticle-stacked micro/nanowire arrays are left on the substrate (Fig. 1f). To gain a deeper and more detailed understanding of this assembly process, we use a heating stage with a light hole to directly observe the entire process under a microscope. As shown in Fig. 1g–i, driven by the capillary force, the liquid quickly filled discrete channels (Fig. 1g). At an appropriate temperature, with the gradual evaporation of water molecules of the dispersion, the liquid with a concave surface moved to the ends of the microchannels, leaving two deposition tails on the side walls (Fig. 1h). With the liquid moving forward, the gold nanoparticles were finally deposited on the side walls of the microchannels. When the evaporation process completed (Fig. 1i) and the PDMS template was peeled off, the aligned nanoparticle-stacked micro/nanowires remained on the substrate. It took only a few seconds to complete the nanoparticle assembly process.

The optical microscopy and scanning electron microscopy images presented in Fig. 2a and b show that the gold nano-

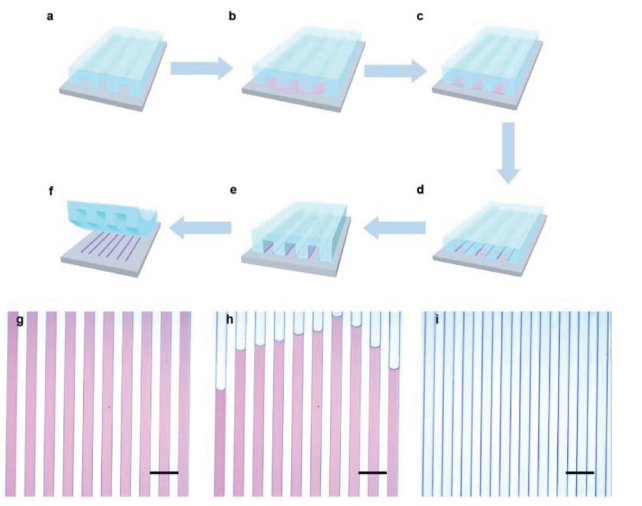

Fig. 1 (a–f) Schematic illustration of the fabrication process of micro/nanowires by the imprinting method. (g–i) *In situ* observation of the assembly process through a microscope at different stages: t = 0 s, (g); t = 27 s, (h); t = 59 s, (i). Scale bars: 50 μm.

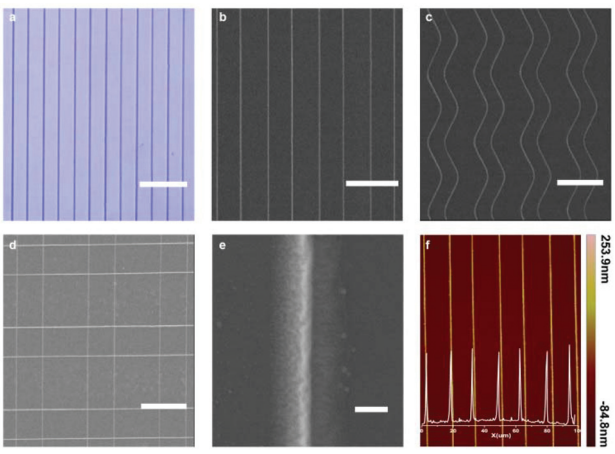

Fig. 2 Characterization of the assembled gold micro/nanowires. (a) Optical microscopy image of assembled gold microwire arrays. SEM images of (b) assembled gold microwire arrays and (c) curved microwire arrays. (d) Network structures obtained by sequential printing. (e) High-magnification SEM image of the microwire. (f) AFM image of microwire arrays. Scale bars: (a) 50 μm, (b) 34 μm, (c) 25 μm, (d) 36 μm, and (e) 750 nm.

particles in the dispersion had been successfully assembled into densely stacked micro/nanowire arrays. From the magnified scanning electron microscopy graph, it could be observed that the micro/nanowires have a uniform width, a smooth surface, and a triangular side structure (Fig. 2e and Fig. S1†). By simply changing the microchannel patterns of the PDMS template, the patterns of the fabricated micro/nanowire arrays can be easily tuned. As shown in Fig. 2c, we can easily fabricate curved microwire array patterns by changing the design of the template pattern. The bending angle of the curved lines is up to 120°, and no obvious defects or breakpoints can be observed at the bending points, demonstrating a high-quality micro/nanowire structure. In addition, we can also regulate the spacing between the micro/nanowires by adjusting the intervals and widths of template microchannels. As shown in ESI Fig. S2,† we have obtained micro/nanowire arrays with different intervals (from 5 μm to 35 μm or even 50 μm) by simply changing the intervals and widths of template microchannels. Such an easy and direct method makes it easily applied to devices with different conductivity or transparency requirements. Different conductivities and transparencies were achieved by changing the intervals of the micro/nanowire arrays, as shown in ESI Fig. S3.† By sequential printing on the already prepared micro/nanowire patterns, we can obtain network structures as shown in Fig. 2d. From the atomic force microscopy image in Fig. 2f, the gold nanoparticle densely stacked micro/nanowires are evenly patterned, with uniform height, width and intervals. Different from the disorderly gold nanowires obtained by the traditional method, the micro/nanowires fabricated by this method are very straight and strictly aligned because of the confinement of the templates. This is very beneficial for their anisotropic properties and can extend their application to anisotropic devices. The length of the micro/nanowires can be adjusted by tuning the length of the template from several micrometers to even millimeters, which can meet different device size requirements. Therefore, our method is suitable for a large-area fabrication process, as shown in ESI Fig. S4,† and aligned gold nanoparticle densely stacked-microwire arrays with an area of over 3 cm × 3 cm were fabricated.

We noticed that the width and thickness of the assembled gold micro/nanowires could be readily tuned by changing the number of nanoparticles that were filled in the microchannels. The number of nanoparticles in the microchannels mainly depends on two factors: the concentration of the filled dispersion and the volume of the microchannels. Here we explored the influence of these two factors on the width and thickness of the assembled micro/nanowires. Firstly, we fixed the volume of the template microchannels as a constant, and each time 5 μl of gold nanoparticle dispersion of different concentrations was applied to assemble into micro/nanowires with different heights and thicknesses. As shown in Fig. 3, an atomic force microscope was used to measure the width and thickness of the assembled micro/nanowires. When the concentration of the applied dispersion decreased, the width and thickness of the assembled micro/nanowires decreased accordingly (Fig. 3a and c). When the concentration decreased to 0.6% w/v, it was almost impossible to form complete wire structures. This was consistent with common sense: when the concentration decreased, the number of nanoparticles in the dispersion was smaller, thereby leading to a reduction in both the width and thickness. By changing the depth of the template microchannels, we explored the influence of the volume of the filled liquid on the width and thickness of the assembled micro/nanowires (Fig. 3b). Here we fixed the dispersion concentration at 2% w/v, and the depths of the template microchannels varied from 3.5 μm to 7.8 μm. The width of the obtained micro/nanowires increased from around 800 nm to 2 μm around and the height from around 100 nm to around 300 nm, correspondingly. With the increase in the depths of template microchannels and consequently the increase in liquid volume that was filled in the microchannels, more gold nanoparticles were deposited onto micro/nanowires, thus contributing to wider and larger micro/nanowires. Therefore, by controlling the dispersion concentration and the depth of the template channels, we can tune the height and width of the assembled micro/nanowires to meet the needs of different device preparations.

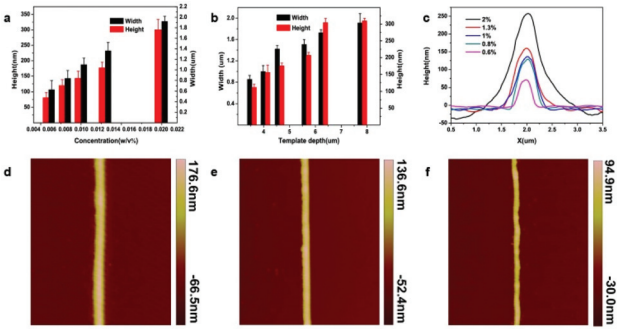

Fig. 3 Different widths and thicknesses of the assembled gold micro/nanowires affected by different parameters: (a) concentrations and (b) different template depths. (c) Height profile image of seven micro/nanowires of different dispersion concentrations. (d–e) AFM images of micro/nanowires of different dispersion concentrations, 1.3% (d); 0.8% (e); 0.6% (f).

We found that the prepared gold micro/nanowires were not electrically conductive, which may be due to two reasons. Firstly, the organic functional groups encapsulated outside the nanoparticles lead to an untight connection among these nanoparticles, which form a significant barrier for electron transportation among these nanoparticles.[23] The low crystallinity of the prepared gold micro/nanowires also hindered the electron transportation within the nanoparticles. So we adopt the high-temperature annealing method to solve these problems. The high temperature annealing process can shorten the distance among the nanoparticles by sintering to enhance the conductivity.[23] At the same time, under high temperature conditions, the organic functional groups that encapsulate the nanoparticles also degrade, further increasing the bonding between the particles, thereby increasing the conductivity. In

addition, the high-temperature annealing can increase the crystallinity of the deposited nanoparticles by promoting grain growth and recrystallization.[24] It has been noticed that the as-prepared assembled micro/nanowires exhibit the indexed peaks of gold. However, after high temperature annealing, the XRD diffraction peaks of the assembled micro/nanowires have a much stronger intensity and a narrower full width at half maximum compared with those of the as-prepared assembled micro/nanowires (ESI Fig. S5†), demonstrating an improvement of crystallinity. At the same time, we found that as the annealing temperature increases, the conductivity of the gold micro/nanowires is indeed enhanced, as shown in ESI Fig. S6 and S7.† Therefore, we chose the gold micro/nanowires after 250 °C of annealing for the preparation of the pressure sensor.

Prior to the application of this gold nanoparticle densely packed microwire-based pressure sensor, the working mechanism was investigated. Since the annealing temperature is around 250 °C, we chose a polymer polyimide with high temperature resistance as the substrate material. Two gold electrode pairs with a gap of 100 μm were evaporated perpendicularly on the micro/nanowire arrays (ESI Fig. S8†). A constant voltage of 0.1 V was applied to the device and the corresponding current was recorded when the external pressure was applied. In Fig. 4, the variations in resistance expressed as $(R - R_0)/R_0$ in response to different outward and inward bending radii are presented. It was noticed that when the device was in an outward bending state (Fig. 4a and d), there was an increasing trend in device resistance, and the larger the bending radius, the higher the device resistance tended to be. Conversely, when the applied pressure bends the device inwardly (Fig. 4c and e), the resistance of the device decreased with the reduction of the bending radius. The pressure induced variation in device resistance mainly originates from the change of connection among the gold nanoparticles of the assembled micro/nanowires. The outward bending state of the device pulls the gold nanoparticles apart from each other, thus leading to fewer electron transportation paths and the increase in the device resistance. In contrast, in an inward bending state, the nanoparticles of the micro/nanowires are compressed closer to each other, contributing to an increase in electron transportation paths, and as a result the device resistance was reduced. There are a tremendous number of nanoparticles in the micro/nanowires, providing a lot of variable contact areas. When a small external pressure was imposed to the micro/nanowire-based device, the accumulation of the variation in the contact area of the numerous nanoparticles produced a rapid and large change in the device resistance, upon which a high sensitive device was fabricated. In addition, even a small pressure as low as 25 Pa can trigger a current variation, as shown in ESI Fig. S9.† This confirms that this gold nanoparticle-based pressure sensor has a high sensitivity and can work in the low pressure range. For practical applications, the device will be under pressure and released repeatedly. As another important factor, the stability of the device was tested by bending outwardly and inwardly many times. As shown in Fig. 4f and g, even after 6000 bending cycles, the device resistance can get back to its initial value with a slight variation around 5%. This feature will facilitate its application to durable devices. The practical application of the device requires that the device has good stability under various conditions. Because gold is an extremely stable metal, it remains very stable in the atmosphere or other conditions. Therefore, our pressure sensor based on gold nanoparticle densely packed micro/nanowires has very high stability. The stability of the device in the atmospheric environment and in humidity is studied. As shown in ESI Fig. S10,† after three weeks under atmospheric conditions, the electrical conductivity of the device has hardly changed. The conductivity of the device remains in its initial state under a relative humidity of 96% for 120 hours. These results show that the device based on gold nanoparticle densely packed micro/nanowires has excellent stability and can work under various conditions.

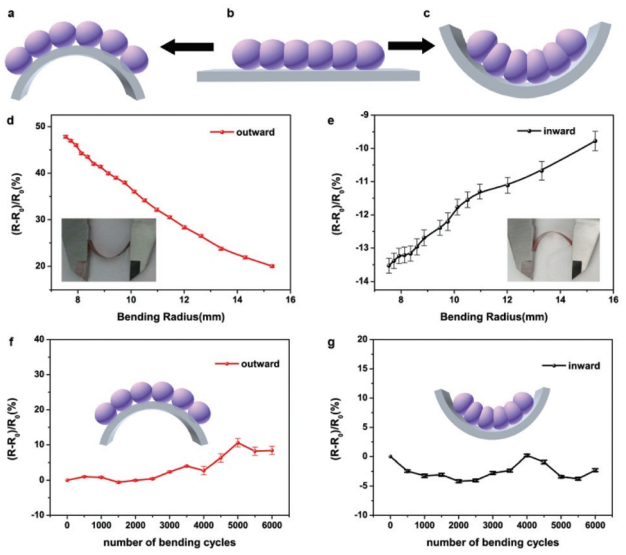

Fig. 4 Working mechanism of the flexible pressure sensor. (a–c) Schematic illustration of different bending states of the assembled micro/nanowires. (d–e) Different variations in resistance in response to different outward (d) and inward (e) bending radii. (f–g) The durability and stability measurement by bending outwardly (f) and inwardly (g) many times.

In order to investigate its capacity to be assembled as wearable pressure sensors for soft robots, artificial intelligence and human movement monitoring, the sensitivity of the device (fabricated at a concentration of 2%) was quantitatively evaluated, as shown in Fig. 5 and ESI Fig. S11a.† The current change of the device in accordance with the applied pressure was recorded to measure the sensitivity. We defined the sensitivity as $S = (I - I_0)/\Delta P \times I_0$, where P is the applied pressure and I and I_0 are the original current without pressure loading and the current after external pressure, respectively. From Fig. 5, determined by the slope of the current curve, different sensitivities were obtained in the different pressure ranges. In the lower pressure range (under 1 kPa), we obtained a sensitivity of

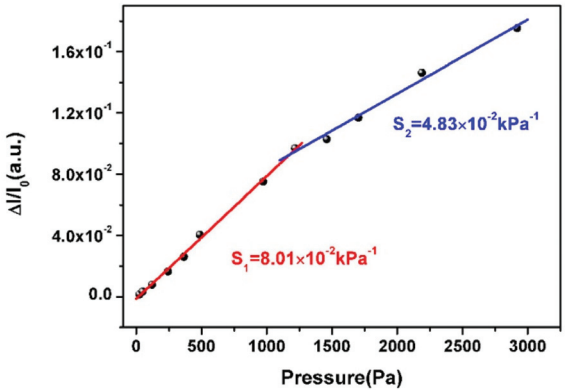

Fig. 5 Relative current change of the pressure sensor during pressure loading.

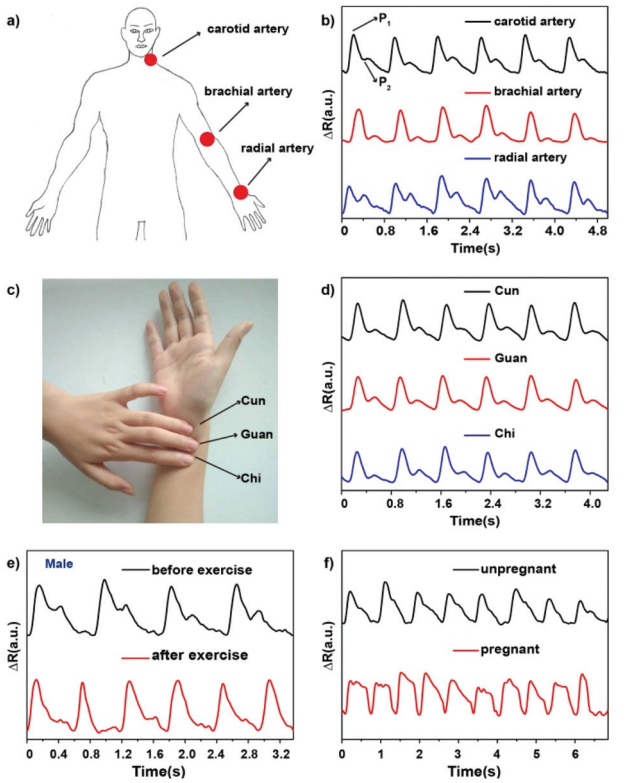

Fig. 6 Artery pulse information monitoring in real time. (a) Several artery regions in the human body. (b) Artery pulse information measured from different regions with our pressure sensor. (c) Locations of Cun, Guan, and Chi acupoints. (d) Waveforms of the Cun, Guan, and Chi acupoints measured by our pressure sensor. Radial artery pulse information of a 24-year-old male (e) and a pregnant woman and a non-pregnant woman (f).

0.08 kPa^{-1}. This confirms that this gold nanoparticle-based pressure sensor has a high sensitivity and can work in the low pressure range. As the applied pressure increased above 1.5 kPa, the sensitivity gradually decreased to 0.048 kPa^{-1}. The reduction in sensitivity in the high pressure range could be explained by the saturation of the change in the connection between the nanoparticles. The sensing performances of the pressure sensors fabricated with different sizes of micro/nanowires were also discussed. As discussed above, we fabricated micro/nanowires with different widths and heights by changing the concentration of the dispersion. The sensitivities of the pressure sensors based on different sizes of micro/nanowires are shown in ESI Fig. S11b and S11c.† With the decrease of the sizes of the micro/nanowires, the sensitivities of the pressure sensors were also decreased accordingly. This may be attributed to the fact that micro/nanowires of smaller size have a smaller number of nanoparticles involved in the sensing process.

Wearable and portable electric devices that can detect biological signals and provide helpful information for medical diagnosis have great importance in the field of modern medicine. In particular, as one of the leading causes of death, cardiovascular disease could be prevented by monitoring the artery pulse signals. Thus a lot of attention has been paid to wearable pressure sensors which can monitor artery pulse information in real time. Based on the analysis above, the pressure sensor based on these gold nanoparticle densely packed micro/nanowires was applied to detect artery pulse signals, as shown in Fig. 6. It was very clear that the artery pulse waveforms showed two distinct peaks P_1 and P_2 (Fig. 6b). P_1 represents the sum of the forward travelling wave and reflected wave, and P_2 denotes the reflected wave from the lower body subtracted by the end-diastolic pressure. Useful parameters can be obtained according to the two peaks, such as the radial augmentation index ($AI_r = P_2/P_1$) and $\Delta T_{DVP}(= T_{P_2} - T_{P_1})$. Because of the flexibility, the pressure sensor can be easily attached to a variety of artery parts of the human body such as the carotid artery on the neck, the brachial artery on the medial side of the arm, and the radial artery on the wrist (Fig. 6a). The output pulse waveforms are clear and slightly different from each other (Fig. 6b), indicating that this pressure sensor is adaptable to various body regions and can effectively sense the slight differences of the artery pulse waveforms in different regions. According to Traditional Chinese Medicine, waveforms of the three different acupoints located at the radial artery region which was named Cun, Guan, and Chi respectively (Fig. 6c) provide substantial information for medical diagnosis. Thus measurements of the waveforms of the Cun, Guan, and Chi acupoints are very important. As shown in Fig. 6d, waveforms corresponding to the three acupoints were effectively measured and recorded. The differences of the waveforms and peak positions were clearly distinguished and could provide useful information for disease diagnosis. As shown in Fig. 6e and ESI Fig. S12,† the radial artery pulse of two testers (a 24-year-old male and a 27-year-old female) before and after exercise was monitored. From the pulse waveforms, we noticed that the heart rate was faster after exercise. For the male tester, the heart rate increased from ≈75 bpm to ≈102 bpm, and AI_r decreased from 0.43 to 0.26 after exercise. And for the female tester, the heart rate increased

from ≈72 bpm to ≈107 bpm, and the AI_r decreased from 0.46 to 0.29 after exercise. For the two testers, the decrease of P_2 was caused by the dilated muscular arteries and reduction of arterial pressure augmentation after exercise. To monitor and distinguish the pulse of pregnant women is very meaningful for medical devices. Our device is so sensitive that it can be used to distinguish the pulse signals of pregnant women and non-pregnant women. In Fig. 6j, the real-time pulse signals of a pregnant woman and a non-pregnant woman are presented. It is clear that the pulse frequency of the pregnant woman (91 bpm) is higher than that of the non-pregnant woman (75 bpm). In addition to frequency, the pulse waveform of the pregnant woman is completely different from that of the non-pregnant woman. The above results demonstrate that pressure sensors based on these gold nanoparticle densely packed micro/nanowires can monitor the human artery signals successfully and hence could be utilized for wearable medical applications.

To evaluate its capability of human activity monitoring, the pressure sensor was affixed to several regions of the human body to record body movements in real time, as shown in Fig. 7. Firstly, the pressure sensor was attached to the second knuckles of the forefinger to monitor its bending movements, as shown in Fig. 7a. When the finger bent, the contact area of the nanoparticles would change accordingly, leading to different output signals. Different resistance changes were outputted in response to different bending degrees of the finger. The device was attached to the wrist and the opisthenar to detect their movements. As shown in Fig. 7b and c, different responsive signals in accordance with different bending angles can be observed. Due to its wide range of work pressure, slight movements such as muscle movements of the throat can also be detected. We attached the pressure sensor to the throat to detect the vibration signals of muscle movements when the tester said different words. As shown in Fig. 7d, when different phrases and words such as “thank you”, “you are welcome”, “hello”, and “I am fine” were pronounced by the tester, the pressure sensor exhibited different waveforms accordingly, demonstrating that the pressure sensor could not only be used to detect voice signals but also to distinguish different words. Each word or phrase was repeated three times and similar waveforms were obtained for the same words and phrases, confirming the excellent reliability of the pressure sensor.

The aforementioned investigations have successfully demonstrated the pressure sensor’s capabilities of wearable components for several practical applications. Here we attached the pressure sensor to the human hand to feedback the dynamic responses in real time when grabbing and moving an object. Variations of the outputted current were observed as the hand grabbed an apple and released it. The current increased rapidly as the grasping motion occurred, and quickly decreased to the normal state when the apple was released, as shown in Fig. 7e and f and ESI Movie S1.† As the sensor was attached to different fingers, different pressure responses of these fingers could be distinguished precisely

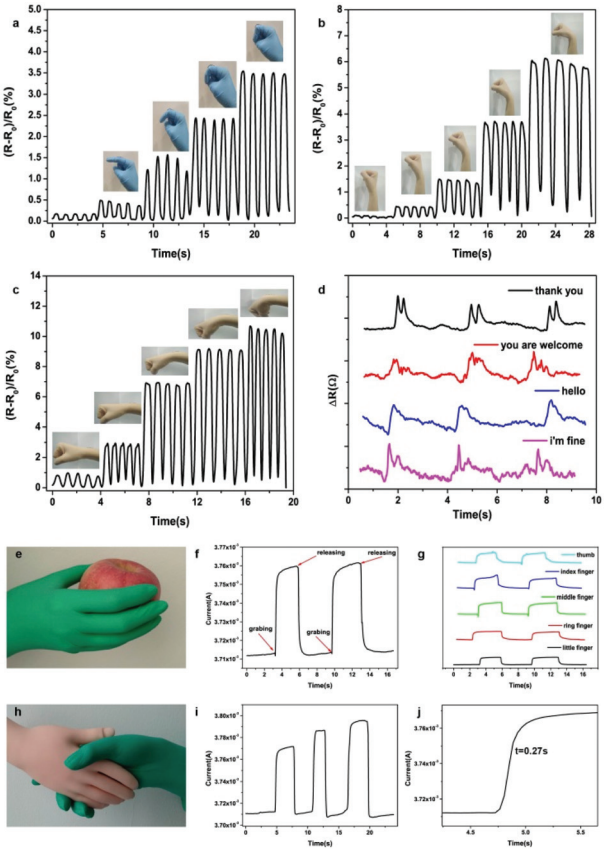

Fig. 7 Detection of several human body movements and an artificial hand by the assembled micro/nanowire-based pressure sensor. Optical images and current signals of the pressure sensor when it is attached to the (a) forefinger, (b) opisthenar, (c) wrist, and (d) throat. (e) Photograph of a human hand attached with the pressure sensor while grasping an apple. (f) Current response of the pressure sensor when an apple was grabbed and released. (g) Different current responses of different fingers while grabbing and releasing an apple. (h) Photograph of a human hand shaking hands with the pressure sensor attached artificial hand. (i) Different current signal responses when shaking hands with the pressure sensor attached artificial hand at different pressures. (j) High resolution current responses of the pressure sensor.

during the grabbing and releasing process, as shown in Fig. 7g. We also attached the pressure sensor to an artificial hand as smart sensing, as shown in Fig. 7h. The pressure induced by hand shaking was monitored in real time by the attached pressure sensor. Fig. 7i shows the dynamic current responses when a tester shook hands with the artificial hand with three different pressures. The responses were not only sensitive but also timely. As shown in Fig. 7j and ESI Fig. S13,† the response and relaxation time of the pressure sensor are 0.27 s and 0.11 s, respectively.

All the mentioned operations were conducted at a very low voltage, and the energy consumption was below 0.8 mw. We can still lower the value by further reducing the working voltage. All the results we discussed above prove that the fabricated pressure sensor has a wide range of applications for wearable sensing units.

Conclusions

In this paper, a pressure sensor based on gold nanoparticle-densely packed micro/nanowires was fabricated. Gold nanoparticles were effectively assembled into highly aligned micro/nanowires by the imprinting method, and the pressure sensor based on these gold micro/nanowires was successfully developed. Due to the excellent properties of the assembled gold micro/nanowires, the pressure sensor exhibits a high sensitivity, low detection limit (25 Pa), and low energy consumption (<0.8 mW), extending its range of practical applications. These excellent properties of the pressure sensor guarantee its application in real-time monitoring of human daily movements and being used as electronic skin for artificial limbs. Based on the simple and low-cost fabrication process, outstanding performance and flexible properties, we provide a new path to smart sensing devices.

Experimental

Materials

(11-Mercaptoundecyl)tetra(ethylene glycol) functionalized gold nanoparticle water dispersion was purchased from Sigma-Aldrich Co. (St Louis, MO) and used as received. The Sylgard 184 Silicone Elastomer kit (including monomer and curing agent) was purchased from Dow Corning.

Preparation of photoresist master mold

A Si wafer was cleaned with acetone, ethanol, and deionized water in turn and dried in an oven right before use. In order to increase the adhesion of photoresist patterns on the Si substrate, the Si substrate was firstly modified by spin-coating the photoresist (SU-8) on it followed by UV irradiation to be fully cured. After this modification procedure, another layer of photoresist (SU-8) was spin-coated on the modified Si substrate at a speed of 2500 rpm for 30 s and baked in an oven at 95 °C for 15 minutes. After UV exposure through a shadow mask for 3 seconds, the substrate with cured photoresist patterns was baked at 95 °C for 5 minutes. By immersing the substrate into a developer for about 1 minute, photoresist patterns were obtained and then further cured through another UV exposure for 5 minutes to make the patterns stick to the substrate more firmly.

Preparation of the patterned PDMS template

The PDMS precursor and curing agent were mixed at a ratio of 10 : 1 (w/w) and stirred until well mixed. After degassing by centrifuging for 8 minutes, the mixture was poured onto the Si mold and cured at 95 °C for 90 minutes. After being fully cured, PDMS templates were obtained by carefully peeling off from the Si master mold.

Characterization

The structures of the assembled micro/nanowires were explored *via* scanning electron microscopy (SEM, JEOL JSM-7500F) at an accelerating voltage of 5.0 kV. The height details were explored by atomic force microscopy (AFM, Bruker Corporation) in tapping mode.

Device fabrication and measurement

The pressure sensor was fabricated by vacuum evaporation deposition of two gold electrodes on the assembled gold nanoparticle densely packed micro/nanowires, and two silver wires were pasted on these two electrodes to facilitate subsequent measurements. A vernier caliper was used to control the bending degree of a device when measuring the resistance changes of the device at different bending degrees. At the same time, a source meter was used to test the *I–V* curves, and resistance values were calculated from the obtained *I–V* curves. The electrical signal and performance characterization of the device under pressure was performed by loading objects of different weights and collected through a source meter. The back of the device was affixed with double-sided tape to form a wearable device to be attached on various parts of the human body or on the artificial hand. All electrical signal collection and real-time monitoring were performed using a source meter (Keithley, 2635B system) at 0.1 V.

Conflicts of interest

The authors declare no competing financial interest.

Acknowledgements

This work was supported by the National Key Research and Development Program of China and the National Natural Science Foundation of China (NSFC) under Grants #61435005, #51335008, # 61590930, 2017YFB1104300, Grant 61605055.

References

1 J.-N. Wang, Y.-Q. Liu, Y.-L. Zhang, J. Feng, H. Wang, Y.-H. Yu and H.-B. Sun, *Adv. Funct. Mater.*, 2018, **28**, 1800625.
2 M. Song, M. Xiao, L. Zhang, D. Zhang, Y. Liu, F. Wang and F. Shi, *Nano Energy*, 2016, **20**, 233–243.
3 X. Yang, M. Cheng, L. Zhang, S. Zhang, X. Liu and F. Shi, *Adv. Mater.*, 2018, e1803125, DOI: 10.1002/adma.201803125.
4 M. Jian, C. Wang, Q. Wang, H. Wang, K. Xia, Z. Yin, M. Zhang, X. Liang and Y. Zhang, *Sci. China Mater.*, 2017, **60**, 1026–1062.
5 Y. Zang, F. Zhang, C.-a. Di and D. Zhu, *Mater. Horiz.*, 2015, **2**, 140–156.
6 S. T. Han, H. Y. Peng, Q. J. Sun, S. Venkatesh, K. S. Chung, S. C. Lau, Y. Zhou and V. A. L. Roy, *Adv. Mater.*, 2017, **29**, 22.
7 D. Yin, N.-R. Jiang, Y.-F. Liu, X.-L. Zhang, A.-W. Li, J. Feng and H.-B. Sun, *Light: Sci. Appl.*, 2018, **7**, 35.

8 X. Wang, Z. Liu and T. Zhang, *Small*, 2017, **13**, 25.
9 Y. Pang, K. Zhang, Z. Yang, S. Jiang, Z. Ju, Y. Li, X. Wang, D. Wang, M. Jian, Y. Zhang, R. Liang, H. Tian, Y. Yang and T. L. Ren, *ACS Nano*, 2018, **12**, 2346–2354.
10 X. Xu, R. Wang, P. Nie, Y. Cheng, X. Lu, L. Shi and J. Sun, *ACS Appl. Mater. Interfaces*, 2017, **9**, 14273–14280.
11 W. Liu, N. Liu, Y. Yue, J. Rao, F. Cheng, J. Su, Z. Liu and Y. Gao, *Small*, 2018, **14**, e1704149.
12 L. Q. Tao, K. N. Zhang, H. Tian, Y. Liu, D. Y. Wang, Y. Q. Chen, Y. Yang and T. L. Ren, *ACS Nano*, 2017, **11**, 8790–8795.
13 N. Luo, Y. Huang, J. Liu, S. C. Chen, C. P. Wong and N. Zhao, *Adv. Mater.*, 2017, **29**, 40.
14 G. Hergert, J. Vogelsang, F. Schwarz, D. Wang, H. Kollmann, P. Groß, C. Lienau, E. Runge and P. Schaaf, *Light: Sci. Appl.*, 2017, **6**, e17075.
15 J. Sun, X. Liu, Q. Tang, J. P. Hill, K. Ariga and Q. Ji, *ChemistrySelect*, 2017, **2**, 5793–5799.
16 V. Chegel, O. Rachkov, A. Lopatynskyi, S. Ishihara, I. Yanchuk, Y. Nemoto, J. P. Hill and K. Ariga, *J. Phys. Chem. C*, 2012, **116**, 2683–2690.
17 J. Vieaud, J. Gao, J. Cane, M. Stchakovsky, A. En Naciri, K. Ariga, R. Oda, E. Pouget and Y. Battie, *J. Phys. Chem. C*, 2018, **122**, 11973–11984.
18 F. Pincella, K. Isozaki and K. Miki, *Light: Sci. Appl.*, 2014, **3**, e133–e133.
19 R. Khandelia, S. Bhandari, U. N. Pan, S. S. Ghosh and A. Chattopadhyay, *Small*, 2015, **11**, 4075–4081.
20 Q. Yu, P. Gao, K. Y. Zhang, X. Tong, H. Yang, S. Liu, J. Du, Q. Zhao and W. Huang, *Light: Sci. Appl.*, 2017, **6**, e17107.
21 L. Wang, Q. D. Chen, X. W. Cao, R. Buividas, X. Wang, S. Juodkazis and H. B. Sun, *Light: Sci. Appl.*, 2017, **6**, e17112.
22 J. Mao, W. E. I. Sha, H. Zhang, X. Ren, J. Zhuang, V. A. L. Roy, K. S. Wong and W. C. H. Choy, *Adv. Funct. Mater.*, 2017, **27**, 1606525.
23 J. Lyu, X. Wang, L. Liu, Y. Kim, E. K. Tanyi, H. Chi, W. Feng, L. Xu, T. Li, M. A. Noginov, C. Uher, M. D. Hammig and N. A. Kotov, *Adv. Funct. Mater.*, 2016, **26**, 8435–8445.
24 L.-J. Huang, N.-F. Ren, B.-J. Li and M. Zhou, *Acta Metall. Sin. (Engl. Lett.)*, 2015, **28**, 281–288.